

# Functionalization of PLLA with Polymer Brushes to Trigger the Assembly of Fibronectin into Nanonetworks

Mark Robert Sprott, Gloria Gallego-Ferrer, Matthew J. Dalby, Manuel Salmerón-Sánchez,\* and Marco Cantini\*

Poly-L-lactic acid (PLLA) has been used as a biodegradable polymer for many years; the key characteristics of this polymer make it a versatile and useful resource for regenerative medicine. However, it is not inherently bioactive. Thus, here, a novel process is presented to functionalize PLLA surfaces with poly(ethyl acrylate) (PEA) brushes to provide biological functionality through PEA's ability to induce spontaneous organization of the extracellular matrix component fibronectin (FN) into physiological-like nanofibrils. This process allows control of surface biofunctionality while maintaining PLLA bulk properties (i.e., degradation profile, mechanical strength). The new approach is based on surface-initiated atomic transfer radical polymerization, which achieves a molecularly thin coating of PEA on top of the underlying PLLA. Beside surface characterization via atomic force microscopy, X-ray photoelectron spectroscopy and water contact angle to measure PEA grafting, the biological activity of this surface modification is investigated. PEA brushes trigger FN organization into nanofibrils, which retain their ability to enhance adhesion and differentiation of C2C12 cells. The results demonstrate the potential of this technology to engineer controlled microenvironments to tune cell fate via biologically active surface modification of an otherwise bioinert biodegradable polymer, gaining wide use in tissue engineering applications.

## 1. Introduction

Biomaterials can be used in tissue engineering to regenerate, replace or supplement in situ biological functions. Polymer-based

M. R. Sprott, Prof. M. J. Dalby, Prof. M. Salmerón-Sánchez, Dr. M. Cantini  
Centre for the Cellular Microenvironment

University of Glasgow  
Glasgow G12 8LT, UK

E-mail: Manuel.Salmeron-Sanchez@glasgow.ac.uk;  
Marco.Cantini@glasgow.ac.uk

Prof. G. Gallego-Ferrer  
Center for Biomaterials and Tissue Engineering  
Universitat Politècnica de València  
Valencia 46022, Spain

Prof. G. Gallego-Ferrer  
Biomedical Research Networking Center in Bioengineering  
Biomaterials and Nanomedicine (CIBER-BBN)  
Valencia 46022, Spain

 The ORCID identification number(s) for the author(s) of this article can be found under <https://doi.org/10.1002/adhm.201801469>.

© 2019 The Authors. Published by Wiley-VCH Verlag GmbH & Co. KGaA, Weinheim. This is an open access article under the terms of the Creative Commons Attribution License, which permits use, distribution and reproduction in any medium, provided the original work is properly cited.

The copyright line for this article was changed on 4 February 2019 after original online publication.

DOI: 10.1002/adhm.201801469

biomaterials especially provide a versatile platform to develop systems for medical purposes due to simple processing.<sup>[1]</sup> Current biomedical research utilizes modification of biodegradable polymers to manufacture implantable microenvironments, which present biochemical signals,<sup>[2]</sup> optimal topologies, and mechanical properties suitable for a specific damaged tissue.<sup>[1b,3]</sup> However, many approved polymer systems lack specific bioactivity; therefore, they do not promote tissue regeneration and are thus limited.<sup>[1b,3a]</sup>

While many surface modification techniques have been developed over the years, surface-initiated atomic transfer radical polymerization (SI-ATRP) has emerged as a methodology for controlled alteration of surface properties for biomedical applications.<sup>[4]</sup> Compared to other surface modification techniques, activator regenerated electron transfer (ARGET) SI-ATRP is tolerant of slight impurities,<sup>[2,5]</sup> such as oxygen, and does not require the same extreme experimental conditions necessary for ionic and ring

opening metathesis polymerization.<sup>[6]</sup> Due to the versatility and variability of SI-ATRP, it can be carried out in many different solvents with a range of temperatures and reagents;<sup>[7]</sup> this makes it an attractive surface modification methodology in biomedical research.<sup>[2,6,8]</sup> SI-ATRP is performed by initially immobilizing initiating groups onto the surface that needs to be modified. If no functional groups are readily available for this immobilization reaction, the base polymer is first modified to present an adequate density of suitable functional groups;<sup>[7]</sup> initiators, for example, bromine-based, can then be favorably immobilized onto the surface in place of the previously added functional groups.<sup>[8b]</sup> The initiators are then catalytically acted upon by ligands that provide the reduction potential for the polymerization of monomers at the surface. The polymer formed is therefore grown from and bound to the surface of the base material, resulting in a nanometric layer of grafted polymer chains.<sup>[8]</sup> These are tethered or end-grafted to the supporting substrate surface in a brush-like conformation;<sup>[8b]</sup> we have henceforth called the SI-ATRP grafted polymers “polymer brushes.” The specificity of the reaction allows for refined control over the molecular weight and functionality of the polymers produced from ARGET SI-ATRP on many different substrates,<sup>[9]</sup> including proteins, inorganic materials, and organic surfaces.<sup>[8b]</sup> Unlike

other surface modification techniques, such as plasma treatment, conventional radical polymerization or UV irradiation,<sup>[10]</sup> SI-ATRP allows controlled incorporation of a complete functional polymer chain onto a surface without significantly altering the chemical and mechanical characteristics of the host material.<sup>[2,11]</sup>

Poly-L-lactic acid (PLLA) is an established biodegradable polymer in biomedical engineering due to key characteristics such as its availability,<sup>[12]</sup> biocompatibility, processability (e.g., for 3D printing), and controlled degradation.<sup>[13]</sup> However, while it provides good mechanical support in damaged tissues, it is not bioactive as it provides limited cellular adhesion and thus does not induce tissue repair through enhanced cell response.<sup>[2,12]</sup> Therefore, PLLA is often modified prior to its application for regenerative medicine purposes.<sup>[12,14]</sup> Here, we propose a novel strategy to add cell adhesive bioactivity to PLLA by incorporating poly(ethyl acrylate) (PEA) brushes onto its surface via SI-ATRP (Figure 1). PEA has the remarkable ability to spontaneously induce material-driven fibrillogenesis of fibronectin (FN), a main component of the extracellular matrix (ECM).<sup>[15]</sup> The surface chemistry of PEA allows for the unfolding of the FN molecule upon adsorption,<sup>[16]</sup> facilitating the presentation of binding sites unavailable in the globular protein; indeed, FN typically adsorbs in globular conformation

on materials such as PLLA.<sup>[17]</sup> However, PEA has been shown to be biostable within the body and is inherently non-biodegradable;<sup>[18]</sup> this limits its use in tissue regenerative applications. By creating a very thin (few nm) layer of PEA on a biodegradable polymer via SI-ATRP,<sup>[19]</sup> the functionality of PEA can be added to a biodegradable system, where the PEA brushes are thin enough to be metabolized.<sup>[20]</sup>

The introduction of PEA brushes (*b*PEA) onto a PLLA surface will allow manufacturing an implantable biodegradable biomaterial, PLLA-*b*PEA, capable of self-organizing FN into nanonetworks that recapitulate the organization of the ECM. This FN unfolding reveals multiple binding domains implicated in the interaction with other ECM components, integrins involved in cell adhesion and growth factors,<sup>[21]</sup> thus enhancing the biological activity of the substrate.<sup>[16,17,22]</sup>

## 2. Results

### 2.1. Characterization of PLLA-*b*PEA

PEA brushes were grown onto PLLA substrates via an optimized ARGET SI-ATRP protocol (Figure 1C). After priming via aminolysis, bromine-based initiators were immobilized on the

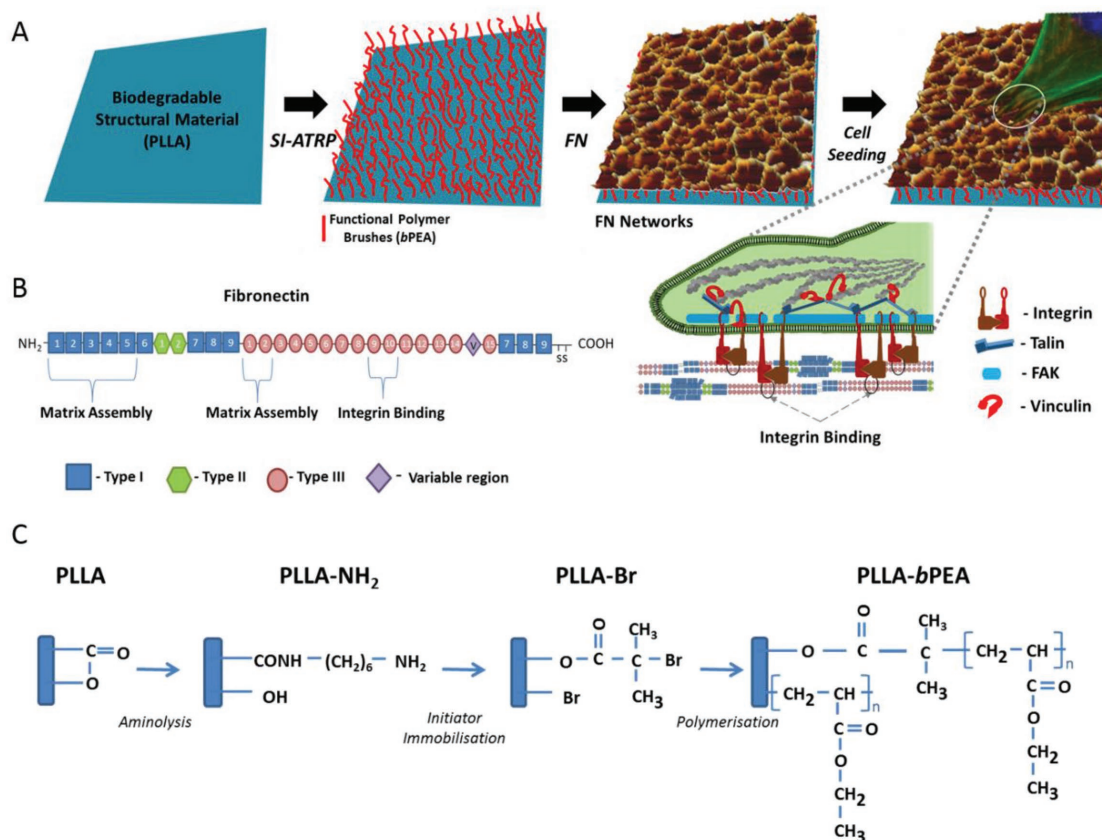


**Figure 1.** Surface modification of PLLA with PEA brushes to induce material-driven assembly of fibronectin into nanonetworks. A) PLLA modified via SI-ATRP to present PEA brushes (*b*PEA) on its surface. PEA drives the assembly of FN into physiological-like nanonetworks that facilitate cell adhesion and differentiation. B) Sketch of FN outlining main matrix assembly and cell binding domains, and representation of the nanofibrils formed upon adsorption on PEA, which expose integrin binding domains and therefore facilitate the formation of focal adhesions by cells. C) Outline of the general methodology of surface modification of PLLA to produce PLLA samples presenting PEA brushes (PLLA-*b*PEA).

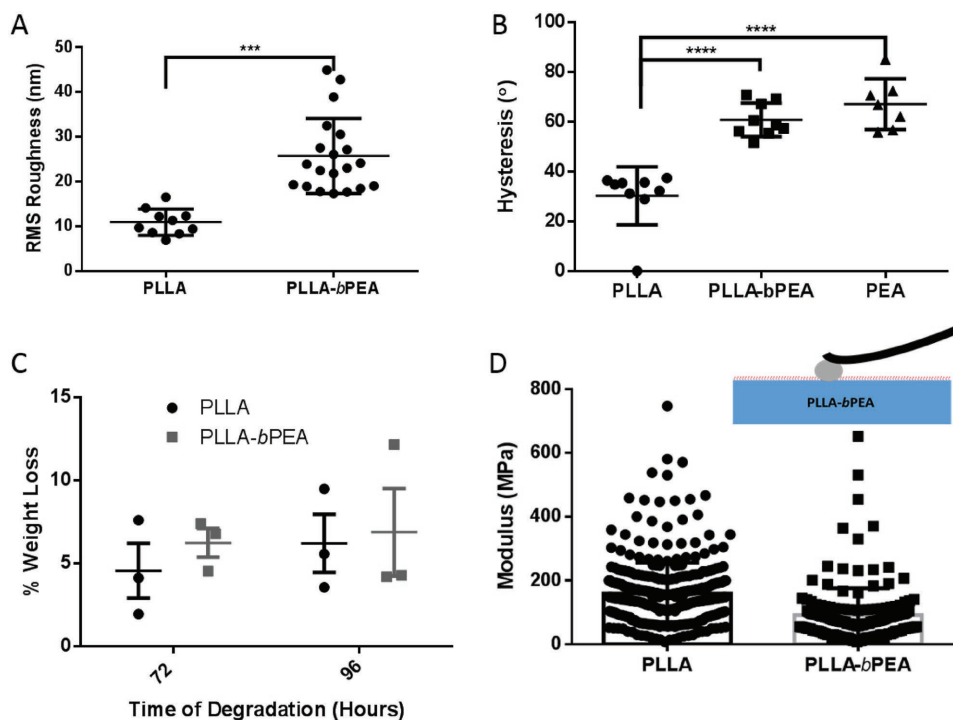


**Figure 2.** Characterization of PLLA-*b*PEA surfaces. A) Surface root mean squared (RMS) roughness measurements of PLLA and PLLA-*b*PEA. Measurements were taken from  $5 \times 5 \mu\text{m}^2$  AFM scans. B) Water contact angle hysteresis of pristine PLLA, PLLA-*b*PEA, and spin-coated PEA samples. C) Percentage weight loss of PLLA and PLLA-*b*PEA measured via nanoindentation in liquid using AFM. Inset shows AFM nanoindentation technique. Graphs show mean values and standard deviation,  $n \geq 3$ . \*\*\* $p < 0.001$ , \*\*\*\* $p < 0.0001$ .

surface; then, ethyl acrylate was polymerized in the presence of low concentrations of a copper catalyst and tris(2-pyridylmethyl) amine (TPMA) ligand, while the reducing agent ascorbic acid was continuously fed into the reaction dropwise. Subsequent characterization of the SI-ATRP treated samples showed that, while topological and chemical alterations were implemented, the bulk properties of PLLA were retained (Figure 2; Figure S1, Supporting Information). In particular, the surface roughness was observed to increase progressively during the SI-ATRP process, from untreated PLLA ( $R_{\text{RMS}} \approx 10.9 \text{ nm}$ ) through initiator immobilization (PLL-Br,  $R_{\text{RMS}} \approx 19.5 \text{ nm}$ ) to the formation of PEA brushes after 4 h of polymerization (PLL-*b*PEA,  $R_{\text{RMS}} \approx 26.0 \text{ nm}$ ) (Figure S1A, Supporting Information; Figure 2A). The first step of the SI-ATRP procedure, aminolysis (PLL-NH<sub>2</sub>), was optimized ( $0.06 \text{ mg mL}^{-1}$  1,6-hexanediamine for 10 min at  $40 \text{ }^\circ\text{C}$ ) to minimize the increase in surface roughness while introducing an adequate surface density of  $-\text{NH}_2$  functional groups ( $\approx 1.6 \times 10^7 \text{ mol cm}^{-2}$ ), calculated from ninhydrin assay (Figure S2, Supporting Information). The changes in surface chemistry were also tracked by measuring the wettability of the samples during the SI-ATRP process; the hydrophobicity was recovered to levels similar to that of bulk PEA samples after formation of the brushes (Figure S1B,C, Supporting Information). Contact angle hysteresis also increased after incorporation of the PEA brushes (Figure 2B).<sup>[23]</sup> The grafting yield, measured by the mass increase after grafting, confirmed that the optimized SI-ATRP protocol produces  $\approx 9 \pm 8 \mu\text{g cm}^{-2}$  of *b*PEA on the PLLA substrate. While we show that the surface

of the PLLA samples was successfully altered to incorporate PEA brushes, it is also important to show that PLLA bulk properties were maintained. Proteinase K was used to hydrolyze PLLA,<sup>[24]</sup> showing similar percentage weight loss after 72 and 96 h of degradation when the surface of PLLA was modified compared to untreated control (Figure 2C). The Young's modulus, measured via nanoindentation in liquid using atomic force microscopy (AFM), was maintained in the MPa range ( $\approx 159$  to  $\approx 91 \text{ MPa}$ ) (Figure 2D). Dynamic mechanical analysis (DMA) confirmed that the bulk mechanical properties of the samples were also in the MPa range ( $\approx 141$  and  $63 \text{ MPa}$ ) (Figure S1D, Supporting Information).

X-ray photoelectron spectroscopy (XPS) was utilized to characterize the surface chemical composition of the top  $<10 \text{ nm}$  of the samples and confirm the incorporation of the PEA brushes (Figure 3; Figure S3, Supporting Information). The carbon and the oxygen spectra (Figure 3A) show distinct differences in the ratio of binding environments in PEA and PLLA; PLLA possesses three main carbon peaks corresponding to carboxyl, ester, and carbon-carbon bonds in a 1:1:2 ratio, whereas PEA possesses a fourth binding environment due to the positioning of the sidechain resulting in a ratio of 1:1:3 producing a much more pronounced peak at  $285 \text{ eV}$  (Figure S3G, Supporting Information). From XPS analysis of products from each step of the SI-ATRP procedure (Figure S3A-E, Supporting Information), we confirmed the introduction of nitrogen peaks after aminolysis (Figure S3B, Supporting Information) and the addition of 2-bromoisobutryl bromide

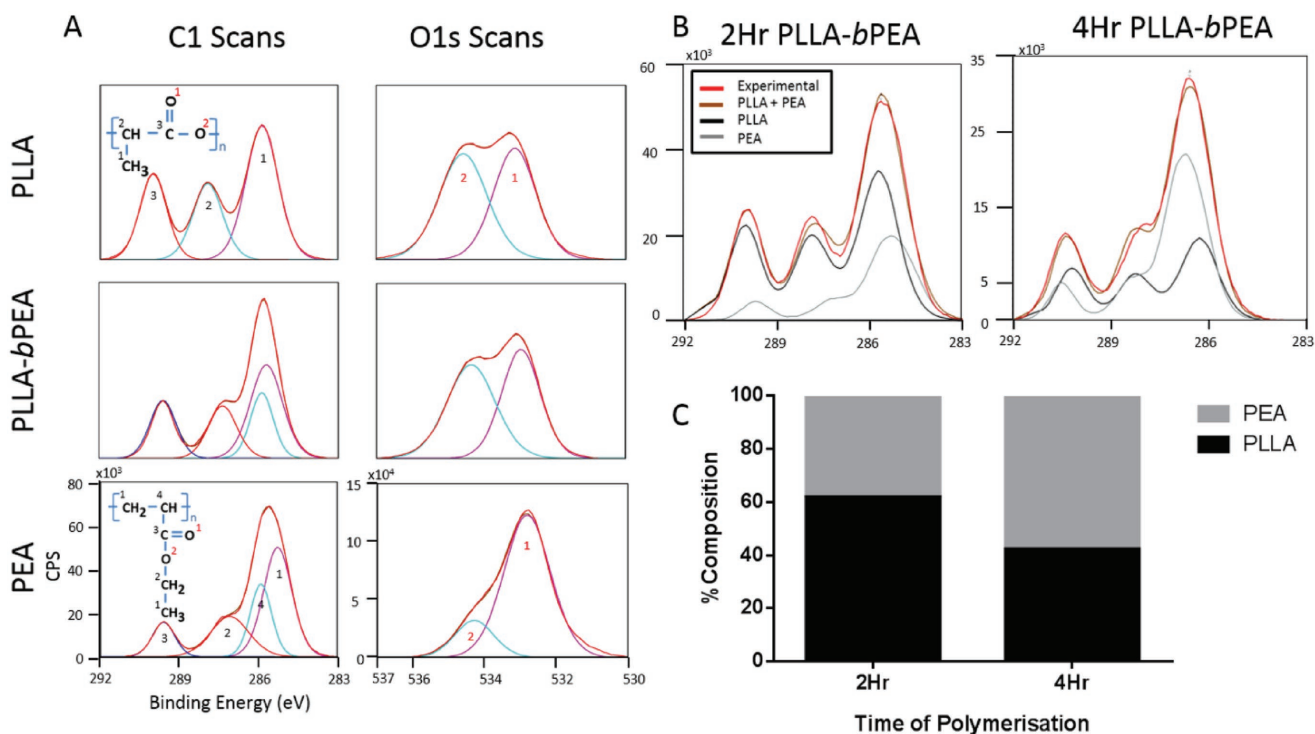


**Figure 3.** Chemical composition of the surface. A) C 1s and O1s core-level spectra of PLLA, PLLA-*b*PEA (after 4 h of polymerization), and spin-coated PEA taken by XPS analysis. Each fitted peak represents a binding conformation of carbon atoms on the top 10 nm of the sample surface. From left to right the carbon peaks represent carboxyl group (COO), ester bond (CO), and carbon to carbon peaks (CC), PEA and PLLA-*b*PEA possess two C–C peaks which represent the polymer backbone carbons with and without sidechains. From left to right the oxygen peaks correspond to the ester bond and carboxyl group within the polymers. Peaks are numerically labeled corresponding to representative chemical structure insets. B) C 1s core-level showing quantification of polymer line-shape elements for PLLA-*b*PEA after a 2 or 4 h polymerization, using the spectra obtained from control PLLA and PEA as components during line fitting. The bright red line corresponds to the experimental spectra for each sample. The line shapes are as follows: black line shows the PLLA carbon spectra, the gray line represents the PEA spectra, brown is the combined spectra of PLLA, PEA. C) The calculated percentage of each polymer component (PEA or PLLA) in PLLA-*b*PEA samples acquired from polymer component peak fitting analysis software.

(BIBB) during the initiator immobilization (Figure S3C, Supporting Information). The bromine to carbon ratio was found to be  $3.4 \times 10^{-3} \pm 1.0 \times 10^{-3}$ ; this indicates a surface density of initiators sufficient to allow continuous brush coverage after polymerization.<sup>[2]</sup> The bromine (Br) peaks found in the Br 3d spectra as a result of the immobilization of BIBB were then removed by the polymerization procedure (Figure S3D, Supporting Information). PLLA-*b*PEA samples possess carbon binding spectra similar to those of PEA, highlighting the chemical modifications of the PLLA surfaces driven by the formation of PEA brushes (Figure 3A). This was further confirmed by analyzing the changes in the XPS spectra during polymerization. Peak fitting the PLLA-*b*PEA spectra with the line shapes of both PLLA and PEA controls allowed estimation of the amount of PEA onto the PLLA substrate, revealing an increase with time from  $\approx 40\%$  after 2 h to  $\approx 60\%$  after 4 h.

## 2.2. Fibronectin Assembly on PLLA-*b*PEA

The ability of the PEA brushes to retain the biofunctionality of bulk PEA was first assessed by studying the interaction of PLLA-*b*PEA samples with FN. AFM imaging confirmed that surfaces modified via SI-ATRP triggered FN assembly upon

adsorption. FN nanonetworks were observed on PLLA-*b*PEA and PEA, while no such structures were formed by FN upon its adsorption on PLLA (Figure 4A and Figure S4 of the Supporting Information for uncoated controls). AFM imaging was performed in ambient conditions, after drying the samples with a gentle nitrogen flow. FN nanofibrils were previously observed in liquid, but further imaging was conducted in air as this improved tip-sample stability allowing easier scanning and better image definition. Indeed, drying was not found to alter the protein distribution, which maintained a fibrillar morphology as similarly observed in liquid on PEA (Figure S5, Supporting Information). The fractal dimension of each image was then calculated and used as a measure of protein network connectivity on the surfaces; FN nanonetworks on both PLLA-*b*PEA and PEA possess fractal properties, with slightly lower levels of interconnection on PEA brushes compared to bulk PEA (Figure 4B). Moreover, this difference in the structural organization of FN observed at the molecular level via AFM translated into a different protein distribution observable at the microscale via fluorescence microscopy of FITC-labeled FN. Indeed, while fibrillar structures were present on PEA and PLLA-*b*PEA, a uniform FN coating was visible on PLLA surfaces (Figure S6, Supporting Information). While the total amount of FN adsorbed was not impacted by the formation of fibrils

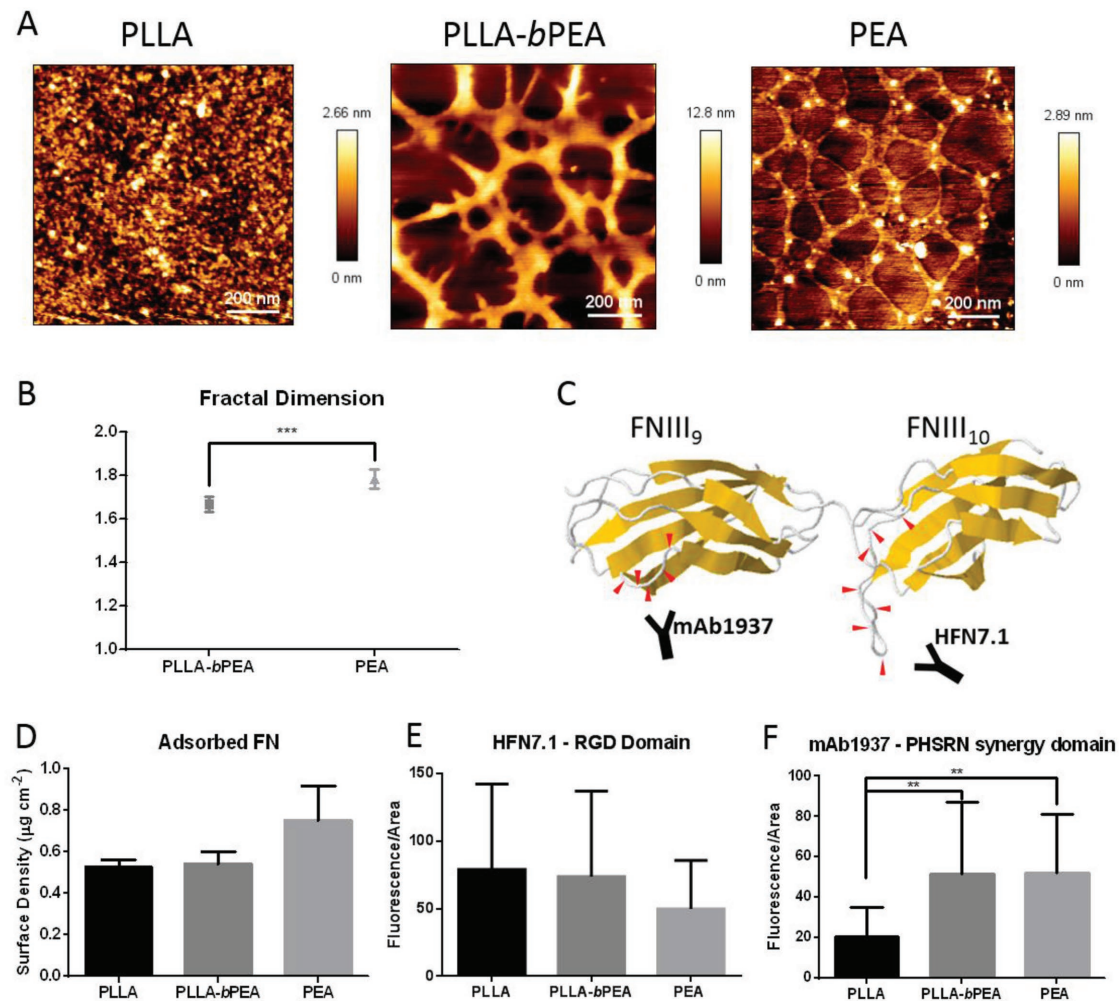


**Figure 4.** Fibronectin adsorption. A) Height images from tapping mode AFM of spin-coated PLLA (scPLLAs), scPLLAs-*b*PEA, and PEA coated with  $20\mu\text{g mL}^{-1}$  FN for 1 h at room temperature. Scale bar is 200 nm. Please note that the color scale is different for every image, as indicated, to allow clear visualization of the surface features. B) Fractal analysis of FN nanonetworks found on scPLLAs-*b*PEA and PEA. C) 3D cartoon of FN integrin binding region (FNIII<sub>9-10</sub>). The binding sequences (PHSRN synergy binding domain, recognized by mAb1937, and RGD binding domain, recognized by HFN7.1) are highlighted by red arrows. Adapted from PDB ID: 1FNF.<sup>[56]</sup> D) Surface density of adsorbed FN on PLLA, PLLAs-*b*PEA, and PEA. E) Quantification of the availability of the integrin binding domain on FNIII<sub>10</sub>, as measured by HFN7.1 binding via ICW. F) Quantification of the availability of the synergy binding domain on FNIII<sub>9</sub>, as measured by mAb1937 binding via ICW. Graphs show mean values and standard deviation,  $n \geq 3$ .  $^{**}p < 0.01$ ,  $^{***}p < 0.001$ .

(Figure 4D), as previously reported,<sup>[17a]</sup> the observed structural difference prompted a differential exposure of integrin binding domains (Figure 4E,F). Indeed, while HFN7.1 binding, which is a measure of the exposure of the RGD domain on FN (Figure 4C),<sup>[22a]</sup> was similar in all conditions (Figure 4E), increased mAb1937 binding (to similar levels as bulk PEA) was observed on PLLAs-*b*PEA (Figure 4F). This implied enhanced exposure of the PHSRN synergy binding domain (Figure 4C), which is a hallmark of the conformational change that occurs with FN fibrillogenesis.<sup>[17a,21,25]</sup>

### 2.3. Cell Adhesion and Differentiation

While C2C12 cells adhered and spread on all surfaces, the actin cytoskeleton appeared more developed on PLLAs-*b*PEA

and PEA, where well-defined stress fibers could be observed, compared to PLLA (Figure 5A), suggesting improved cellular adhesion to surfaces presenting FN nanonetworks. This was further assessed by analyzing the size distribution of the focal adhesions (FAs) formed on each surface using vinculin staining images of single cells (Figure 5A, insets). FAs increased in both number and average size on PEA-containing samples compared to PLLA (Figure 5B,C). In particular, FA size increased from PLLA through PLLAs-*b*PEA to PEA (Figure 5C). The frequency distribution of FA size confirms these results (Figure 5A), as smaller focal adhesion plaques are characteristic of PLLA samples (more than 95% of the FAs are smaller than 2  $\mu\text{m}$ ), while with the formation of FN nanonetworks the percentage of bigger FAs increases ( $\approx 20\%$  and  $\approx 35\%$  of FAs are longer than 2  $\mu\text{m}$  on PLLAs-*b*PEA and PEA, respectively). The cell area was not impacted by the increased presence of elongated

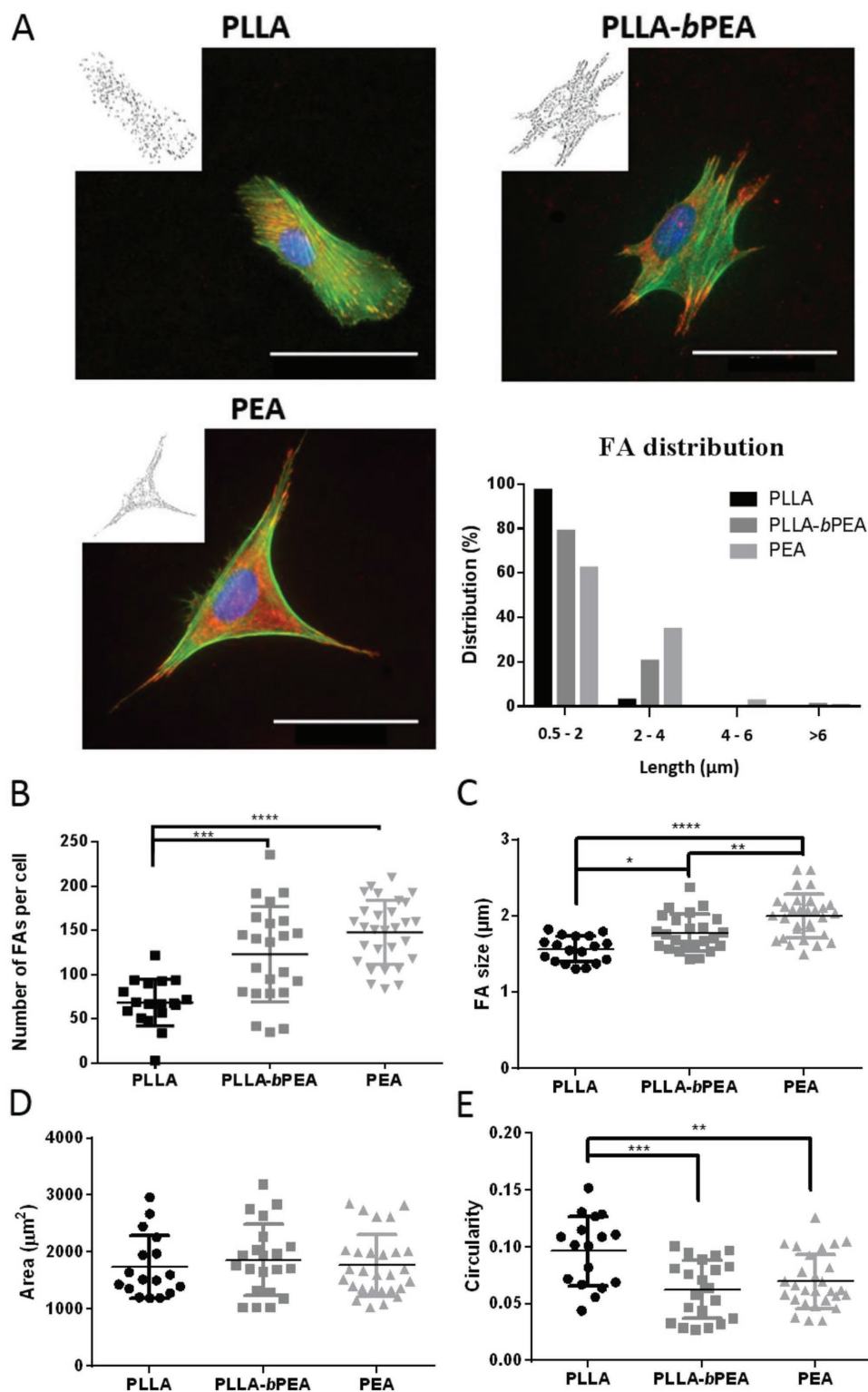


**Figure 5.** Adhesion of C2C12 cells. A) Representative images of focal adhesions formed by C2C12 cells on FN-coated PLLA, PLLA-*b*PEA, and PEA after 4 h of culture and frequency distribution of their size. Samples were stained for actin (green), vinculin (red), and DAPI (blue). The insets show thresholded binary images of the vinculin staining. Scale bar is 50  $\mu\text{m}$ . B) Number of focal adhesions per cell. C) Average focal adhesion size. D) Cell size. E) Cell circularity. Graphs show mean values and standard deviation,  $n \geq 15$ . \* $p < 0.05$ , \*\* $p < 0.01$ , \*\*\* $p < 0.001$ , \*\*\*\* $p < 0.0001$ .

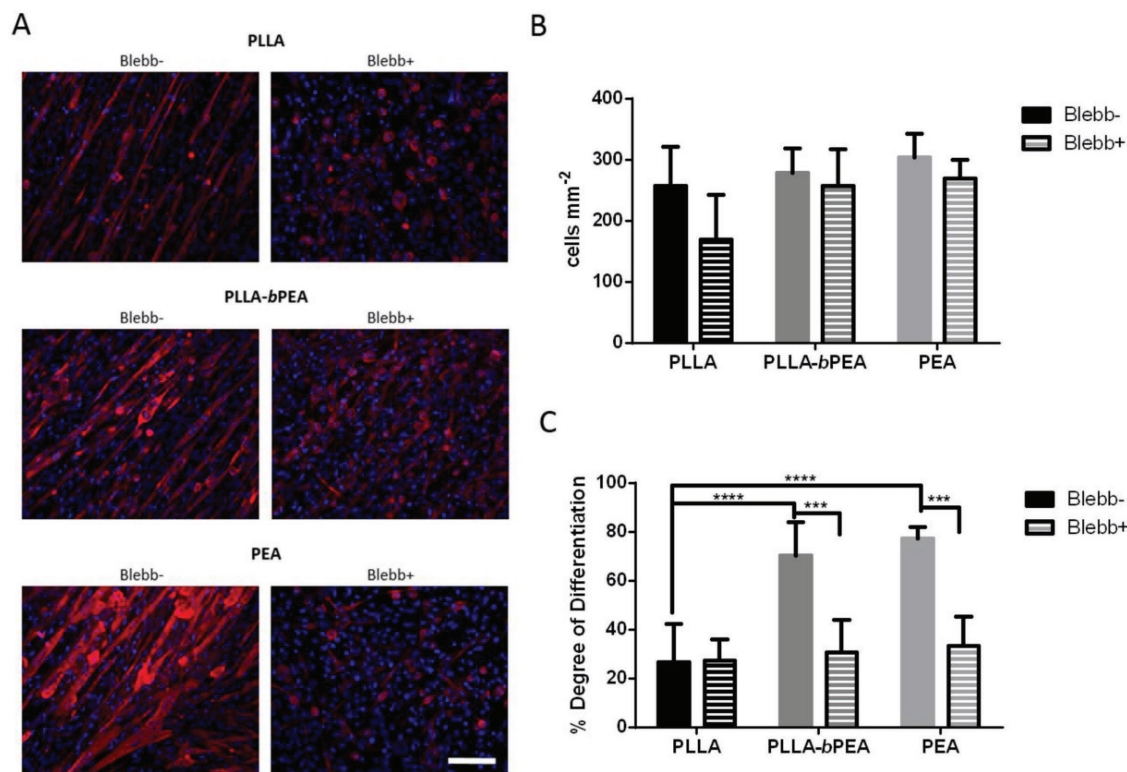


**Figure 6.** Cell differentiation. A) Sarcomeric myosin (red) and nuclei (blue) of C2C12 cells after 4 days of differentiation on FN-coated PLLA, PLLA-*b*PEA, and PEA. Scale bar is 100  $\mu\text{m}$ . B) Cell density. C) Degree of myogenic differentiation measured as percentage of sarcomeric-myosin positive cells. Blebbistatin (Blebb) was used as contractility inhibitor. Graphs show mean values and standard deviation,  $n \geq 4$ . \*\*\*\* $p < 0.001$ , \*\*\*\* $p < 0.0001$ .

FAs (Figure 5D), while the cell circularity was observed to decrease significantly on samples exposing FN fibrils (PEA and PLLA-*b*PEA) (Figure 5E), suggesting a more stellate morphology and confirming morphologies observed in Figure 5A.

Further to adhesion, the differentiation of C2C12 cells toward the myogenic lineage was evaluated by staining for sarcomeric myosin after 4 days in differentiation medium (Figure 6A). Results show that PLLA-*b*PEA supported enhanced levels of cell differentiation (differentiation degree  $\approx 70\%$ ) and myotube formation compared the PLLA (differentiation degree  $\approx 25\%$ ), resembling cell behavior on spin-coated PEA (Figure 6C). The increased degree of differentiation on PLLA-*b*PEA did not result from an increase in cell density, as all samples supported similar cell numbers (Figure 6B). When cell contractility was inhibited via the addition of blebbistatin, a myosin II inhibitor, in the culture medium, cell density was not affected in any condition, while the degree of differentiation dropped to  $\approx 25\%$  for PEA and PLLA-*b*PEA. The level of differentiation achieved for cells on PLLA was instead not affected by the inhibition of contractility via blebbistatin (Figure 6B,C), while cell morphology varied significantly (Figure 6A).

### 3. Discussion

A growing number of studies have sought to improve and control the biological performance of biomaterials through surface modification strategies.<sup>[1b,3a,26]</sup> The approaches have included,

e.g., use of topographical features or chemical alterations to introduce specific functional groups.<sup>[12,27]</sup> The common aim of these surface modifications is to drive cellular behavior toward a desired fate,<sup>[28]</sup> whilst the (possibly biodegradable) bulk substrate supports the mechanical load. For example, nanotopographical features have been shown to modulate stem cell differentiation on otherwise bioinert polymers such as polymethylmethacrylate and polycarbonate.<sup>[27,29]</sup> Plasma polymerization has been used to produce thin polymer coatings on bioinert glass, which drive cell interactions through changes in the activity of the adsorbed protein layer.<sup>[30]</sup> Whilst promising, these strategies present a number of technological challenges. The application of the desired nanotopographical features to 3D structures is a complex engineering task. Plasma polymerization, whilst attractive because it allows depositing thin polymer films independently of the chemical composition of the substrate, often leads to highly crosslinked coatings, to the unwanted loss of functional groups due to the fragmentation of the monomer and to nonuniform coatings when applied to scaffolds.<sup>[31]</sup> Here, we develop a new polymerization strategy that is tuneable, scalable, and ready for translation to complex 3D structures; it allows the introduction of polymer brushes that maintain their functionality onto a structural biodegradable support, such as PLLA. This provides a new platform for the mimicry of in vivo cellular environments.

SI-ATRP, which we optimize in this work for the growth of PEA brushes on PLLA, is a well-documented polymerization technique that allows for a highly tuneable system; it provides

the ability to control initiator density, architecture, surface roughening, polymer chain length, and polydispersity.<sup>[7,8b]</sup> Moreover, the addition of an activator regeneration enzyme minimizes the time, temperature and concentration of reagent requirements associated with the polymerization allowing for greater control during the process.<sup>[32]</sup> This work exploits the features of ARGET SI-ATRP to establish a polymerization technique that allows the controlled production of PEA brushes onto PLLA while maintaining both the functional properties of the acrylate and the structural properties of the PLLA substrate.

Chemical analysis via XPS of the treated surfaces showed that the PEA brushes formed on top of the PLLA substrate closely resembled the composition of bulk PEA controls obtained from photoinitiated radical polymerization of EA (Figure 3A). There is no loss of individual binding environments upon polymerization, a sign of fragmentation of the polymer chain,<sup>[33]</sup> unlike other surface modification techniques such as plasma polymerization. Therefore, intact polymer chains are formed utilizing ARGET SI-ATRP. The carbon spectra of PLLA-*b*PEA possess binding ratios similar to that of PEA while presenting slight variations corresponding to the underlying PLLA backbone, suggesting that the coating is thinner than 10 nm. Optimization of the SI-ATRP protocol allows for control of such factors;<sup>[34]</sup> for example, by increasing time of polymerization the percentage of PEA on the surface can be directly increased as shown in Figure 3C. Other studies have also demonstrated that the tuneability of ATRP allows for the further optimization of the procedures to control brush length and density; for example, the regulation of the reaction kinetics and abundance of initiation sites provides the potential to develop a more definable system.<sup>[35]</sup> In our study, we have modified the PLLA surface to introduce a sufficient surface density of amine groups ( $\approx 1.6 \times 10^7$  mol cm<sup>-2</sup>) and subsequently of bromine-based initiator groups ([Br]/[C] of  $\approx 3.4 \times 10^{-3}$ ) to achieve continuous brush coverage.<sup>[2,36]</sup>

The surface topology was also altered as a result of the functionalization with PEA brushes. The incorporation of the bromine initiator accounted for the largest increase in RMS roughness (Figure S1A, Supporting Information); indeed, the initiator immobilization is an exothermic reaction and the high temperature can stress the base polymer, resulting in its degradation. Secondary aminolysis reactions possibly occurring upon the release of 1,6-hexanediamine within the reaction vessel (as the presence of a nitrogen peak in the XPS spectra after immobilization might suggest, Figure S3C, Supporting Information) might also have a roughening effect. With the subsequent formation of PEA brushes both nitrogen and bromine elements are removed (Figure S3D, Supporting Information) and a rougher surface topology is formed (Figure S1A, Supporting Information); this is compatible with the formation of high density brushes.<sup>[12,37]</sup> Water contact angle (WCA) hysteresis also increased after polymerization (Figure 2B; Figure S1C, Supporting Information), suggesting an increase in molecular mobility due to the presence of the brushes and surface roughening.<sup>[23,38]</sup>

With regards to the maintenance of the bulk characteristics of the PLLA as a structural polymer, both its mechanical properties and degradation were investigated. No significant alterations were observed in PLLA-*b*PEA samples. The degradation

rate was maintained (Figure 2C) and a slight decrease was observed for the Young's modulus, which was still in the MPa range (Figure 2D; Figure S1D, Supporting Information). The Young's modulus was investigated both locally via nanoindentation using AFM and macroscopically via DMA in tension mode. The decrease in stiffness of the polymer observed using both techniques is likely a result of the chemical lysis of the lactide backbone caused by the aminolysis step of the procedure.<sup>[12]</sup> The maintenance of the bulk PLLA degradation rate provides the potential for a PLLA-*b*PEA scaffold to structurally support the tissue to be regenerated after implantation, while gradually reintroducing physical function to cells in situ through tuneable degradation.<sup>[39]</sup> Studies have shown that maintenance of high Young's moduli and degradation characteristics are vital for, e.g., in vivo bone regeneration, due to extended tissue regeneration times in clinical applications.<sup>[40]</sup> As such, the SI-ATRP system developed here provides a highly specific surface modification while minimizing the alteration of the bulk properties of PLLA, improving its biomedical application potential.

The nanometric PEA brushes introduced on the PLLA surface with our methodology retained their characteristic property of inducing surface-initiated fibrillogenesis of FN, as revealed via AFM and immunofluorescence (Figure 4; Figure S6). FN nanonetworks were observed on PLLA-*b*PEA, while only globular clusters were visible on PLLA. The FN fibrils seemed thicker and slightly less interconnected on PLLA-*b*PEA compared to those found on control PEA. Fractal analysis confirmed the slight decrease of interconnection, while the fractal properties of the protein network were maintained (Figure 4A,B).<sup>[41]</sup> The observed differences in the FN nanofibrils assembled on PEA and PLLA-*b*PEA are likely due to the increased roughness and to the brush organization of the surface after ATRP polymerization. FN is in fact a large protein: it has a size of  $\approx 30$  nm when it is in globular conformation in solution,<sup>[42]</sup> and it is few nanometers in diameter with two  $\approx 40$  nm long arms once in an open conformation following interaction with PEA.<sup>[43]</sup> On the other hand, the PEA brushes are only few nanometers high. The adsorption of such a comparatively large molecule is likely to locally disrupt the polymer brush, hindering further protein adsorption in the immediate vicinity of preadsorbed FN molecules and allowing only FN-FN interactions instead. This would favor local fibril growth at the expense of interconnectivity, eventually leading to thicker and less interconnected FN nanofibrils compared to FN adsorbed on flat spin-coated bulk PEA, where the first FN molecules that are adsorbed do not lead to any local disruption of the polymer surface. Besides the different nature of the polymer surface, the increased roughness observed after SI-ATRP might be another factor that plays a role in the alteration of the properties of the FN nanonetwork; nanoroughness is known to affect protein adsorption and might also affect fibrillogenesis.<sup>[44]</sup>

Due to the wide range of cellular interactions that FN mediates in the ECM in vivo, the conformational presentation of this protein is a prime target for tissue engineering.<sup>[21,45]</sup> Previous studies utilizing polymers with varying surface mobility or model surface chemistries (such as polyacrylates with side chains of varying lengths or self-assembled monolayers with defined chemistries) have highlighted the relationship between FN conformation and integrin binding availability.<sup>[17,46]</sup>

These studies have shown that changes in FN conformation and mobility prompted by adsorption on specific material surfaces regulate the exposure of binding domains.<sup>[22a]</sup> For example, structural alterations caused by material-driven fibrillogenesis expose motifs previously unavailable on globular FN,<sup>[16b]</sup> facilitating cellular behaviors such as adhesion and differentiation.<sup>[22a,46b]</sup> FN in its globular conformation is unable to adequately facilitate cellular binding to adhesion and growth factor domains present on the molecule, while when adsorbed on PEA as nanonetworks it exposes these binding sites and enhanced cellular adhesion and signaling occur.<sup>[17a,47]</sup> Previous studies have showed that unmodified semicrystalline PLLA is unable to induce such structural changes in adsorbed FN,<sup>[48]</sup> as we have confirmed here (Figure 4A). Indeed, while HFN7.1 antibodies are able to bind near the RGD domain on globular FN, as found on unmodified PLLA, only the structural conformation change provided by the addition of PEA brushes is able to expose the synergy binding domain recognized by mAb1937 (Figure 4F).<sup>[17a,49]</sup> This definitely shows that the PEA brushes formed through SI-ATRP are functionally active and able to drive FN fibrillogenesis, as found on bulk PEA,<sup>[17a]</sup> notwithstanding the morphological differences in the nanofibrils observed via AFM. PLLA-*b*PEA therefore has the potential to increase the biological activity of bulk PLLA by improving its interfacial interactions with adhesive proteins and cells.

As a result of the change in protein structure, distribution, and conformation, cells were observed to spread better, showing lower circularity, on PLLA-*b*PEA samples, producing a greater number of mature focal adhesion plaques, similar to those found on PEA (Figure 5). These findings correspond to previous research regarding the effect of the formation of FN nanonetworks on acrylate polymers,<sup>[17a]</sup> and further demonstrate that the inclusion of PEA brushes improves bioactivity. The step-wise increase in the number of focal adhesions and in their size (Figure 5B,C) from PLLA through PLLA-*b*PEA to PEA is also in line with the increase in the fractal dimension (Figure 4B).

Finally, PLLA-*b*PEA surfaces were able to induce myogenic differentiation to similar levels as that of bulk PEA (Figure 6), showing that the addition of increased functionality to the PLLA backbone is able to support higher order cellular functions beside the enhanced adhesion.<sup>[39]</sup> Murine myoblast cells (C2C12) were utilized as a cell model due to their general utility and capacity to form myotubes *in vitro*.<sup>[17b,41]</sup> Cell density can impact the degree of differentiation, with increased density inducing higher differentiation in C2C12 cell populations.<sup>[50]</sup> Here, density was maintained between the different conditions, while myotube formation was increased (Figure 6B,C) in the presence of FN nanonetworks. We previously showed the importance of these nanonetworks in driving myogenic differentiation, highlighting that the conformational changes in the molecule are able to enhance the differentiation degree.<sup>[16b,41]</sup> This study confirms that C2C12 differentiation on the nanonetworks is a contractility-dependent process, as the introduction to the media of blebbistatin, a myosin II inhibitor, inhibited differentiation.<sup>[51]</sup> The dependence of cellular differentiation on contractility has been previously reported,<sup>[17b]</sup> indicating that actin-myosin contractility is activated by these physiological-like FN nanofibrils.<sup>[52]</sup> Here we show that the mechanism by which PLLA-*b*PEA is able to regulate and drive cellular differentiation

is also contractility dependent. This paves the way for the use of this system with, e.g., mesenchymal stem cells,<sup>[47,53]</sup> providing a novel biodegradable scaffold for their targeted differentiation and, ultimately, tissue regeneration.

## 4. Conclusion

In this work we have detailed the surface modification of biodegradable PLLA films via the incorporation of functional PEA brushes through SI-ATRP. The PLLA-*b*PEA surfaces are able to drive FN organization into nanonetworks, promoting the availability of binding domains on adsorbed FN and subsequently improving cellular response, in terms of adhesion and differentiation. The novel SI-ATRP process presented here allows for the controlled modification of a biomaterial surface while maintaining its bulk polymer characteristics, such as controlled degradability and mechanical strength. Ultimately, this surface modification strategy provides a simple and scalable technology to improve the biological performance of a structural biodegradable substrate by controlling its interfacial interactions with adhesive proteins and cells. The added functional polymer brushes of PEA can in fact be further employed to target cell response as an efficient tool for the localized presentation of growth factors bound to unfolded FN in complex 3D structures.<sup>[47]</sup>

## 5. Experimental Section

**Materials:** Poly(L-lactide) films (thickness 50  $\mu\text{m}$ ) were purchased from Goodfellow (Huntingdon, UK). 1,6-hexanediamine (98%), 2-propanol ( $\geq 99.5\%$ ), 2-bromoisobutyl bromide (BIBB, 98%), anhydrous pyridine (Py, 99.8%), anhydrous hexane (95%), copper(I) bromide (CuBr, 99.999%), Tris(2-pyridylmethyl)amine (TPMA, 98%), ethyl acrylate (EA, 99.5%), methanol (99.99%), and ascorbic acid (AsAc) were purchased from Sigma-Aldrich, Dorset, UK. Glass reaction vessels were custom-made. Spin-coated PEA controls were prepared on 12 mm glass coverslips from 4% solutions in toluene of bulk PEA, obtained via polymerization of EA using 1% benzoin (Sigma, St. Louis, MO) as a photoinitiator, spun at 3000 rpm with acceleration of 3000 rpm  $\text{s}^{-1}$  and vacuum dried at 60  $^{\circ}\text{C}$  for 2 h to remove excess toluene.

**Preparation of PLLA-*b*PEA Films:** The developed SI-ATRP system takes place in three steps: priming (aminolysis), initiator immobilization (bromination), and polymerization (Figure 1); these processes take place sequentially and separately within different reaction vessels. PLLA films were cut into 13.8 mm circles, with an area of 1.5  $\text{cm}^2$ . The aminolysis protocol was carried out according to the method described in Zhu et al.<sup>[12]</sup> Briefly, PLLA films were immersed in 1,6-hexanediamine and 2-propanol at 40  $^{\circ}\text{C}$  for 10 min. Samples were then washed in deionized water at RT for 24 h with constant agitation to remove excess 1,6-hexanediamine and then vacuum dried at room temperature to a constant weight. A ninhydrin colorimetric method was utilized to quantify the amount of available amine groups bonded onto the surface of the aminolyzed PLLA samples. Samples were immersed in 1 mL of ninhydrin solution, prepared by mixing 40 mL of 0.35 M ninhydrin dihydrate and 4.49 M ninhydrin in ethylene glycol with 10 mL of 0.04 M lithium acetate buffer at pH 5.2. The samples were then heated to 90  $^{\circ}\text{C}$  for 20 min and subsequently diluted with 9 mL of 1:1 2-propanol:deionized water solution. The vials containing the samples were vigorously vortexed to include any chromatic sediments, elutes were pipetted into a 96-well plate and absorbance was read at 566 nm

using Tecan NanoQuant Infinite M200 Pro plate reader (Männedorf, Switzerland). A calibration curve was obtained using solutions containing glycine of known concentrations.

For initiator immobilization, aminolyzed PLLA films were placed on shelves within a three-necked sealed reaction vessel, which was then degassed with oxygen-free nitrogen gas. 3.5 mL BIBB and 70 mL anhydrous hexane were degassed within a side-arm and added to the reaction vessel to fully cover the samples. 1.4 mL pyridine was then dropped slowly into the reaction vessel as the reagents were stirred vigorously with a magnetic stirrer. The overall ratio of the reagents was hexane:BIBB:pyridine [20:1:0.4]. The reaction was maintained at 0 °C with an ice bath for 2 h and then subsequently kept at room temperature (24 °C) for 22 h. A nitrogen flow was maintained throughout the entire 24 h protocol. The initiator immobilized PLLA samples were then removed from the reaction vessel and washed with 2:1 deionized water:methanol solution in a soxhlet apparatus for  $\geq 72$  h and then vacuum dried to constant weight. Polymerization of initiator immobilized PLLA samples was carried out within a separate reaction vessel in a nitrogen atmosphere at room temperature. 1.95 mg CuBr and 12.8 mg TPMA powder were added to the bottom of the reaction vessel containing the PLLA samples. 16.65 g of ethyl acrylate and 16 mL of methanol were then placed in a side arm of the reaction apparatus and the whole vessel was purged with nitrogen. Once all samples were immersed in this solution and thoroughly mixed through, 123.28 mg ascorbic acid dissolved in 16 mL methanol was introduced dropwise (over 1 to 4 h). The final ratio of the reactants was EA:CuBr:TPMA:AsAc [96:0.005:1:0.4]. The polymerization was stopped by flooding the vessel with oxygen and the samples (PLLA-*b*PEA) were then washed in 2:1 deionized water:methanol solution within a soxhlet apparatus for  $\geq 72$  h and vacuum dried to constant weight. For the measurement of grafting yield samples were weighed before and after SI-ATRP treatment using an Ohaus Pioneer balance; grafting yield was calculated as  $(W_{\text{PLLA-}b\text{PEA}} - W_{\text{PLLA}}) / A$ , where  $A$  is the film area (30 samples of  $\approx 1$  cm<sup>2</sup>).

Spin-coated PLLA samples (scPLLA) were prepared by first treating 12 mm glass cover slips with hexamethyldisilazane and then a 2% PLLA solution in chloroform was spun at 2000 rpm with an acceleration of 3000 rpm s<sup>-1</sup>. scPLLA samples were then aminolyzed as described previously and washed with milliQ water for 6 h and subsequently air dried. Initiator immobilization was performed for 6 h without agitation, samples were then washed with gentle pipetting of water and methanol mix and air dried. Polymerization was performed as before with the exemption of soxhlet washing. scPLLA and scPLLA-*b*PEA were used to observe FN conformation via AFM (Figure 4A).

**Atomic Force Microscopy:** Atomic force microscopy was used to quantify surface roughness and visualize topology before and after FN coating in all conditions on dried samples in air. FN-coated samples were rinsed with water after FN adsorption and gently dried with a nitrogen flow. For AFM imaging of FN in liquid, sample were not dried, but rather washed with Dulbecco's phosphate buffered saline (DPBS) and MilliQ water before being fixed with 4% formaldehyde at room temperature for 20 min. Height and lock-in phase images were taken in AC mode using a Nanowizard 3 Bioscience AFM (JPK, Berlin, Germany). Scans were made using cantilevers with a resonance frequency of 75 kHz and a force constant of 3 N m<sup>-1</sup> (MPP-21120 from Bruker, Billerica, MA). Surface area scans ( $n = 3$ ) of  $5 \times 5 \mu\text{m}^2$  (0.5 Hz) were used to analyze surface roughness of each sample from any given condition. The  $R_{\text{rms}}$  was calculated using the JPK DP software after image leveling to remove variations or tilts in the background. Scans of  $2 \times 2 \mu\text{m}^2$  (0.7 Hz),  $1 \times 1 \mu\text{m}^2$  (0.8 Hz), and  $0.5 \times 0.5 \mu\text{m}^2$  (1 Hz) were used to identify features and qualitatively assess surface topology. Fractal dimension analysis was carried out on the  $1 \times 1 \mu\text{m}^2$  images of FN-coated samples using the ImageJ Fractal box count analysis tool, using box sizes of 2, 3, 4, 6, 8, 12, 16, 32, and 64 pixels.

Force spectroscopy curves were obtained, after calibration of cantilever sensitivity and spring constant, using  $\approx 30$  N m<sup>-1</sup> cantilevers with a 20  $\mu\text{m}$  diameter spheric silica tip. The cantilever was approached to the surface with a constant speed of 2.0  $\mu\text{m}$  s<sup>-1</sup>, at room temperature in water, and the Young's modulus was calculated using a Hertz model (JPK DP software), with an indentation depth of 30 nm.

**Water Contact Angle:** Water contact angle measurements were undertaken on PLLA and functionalized samples. Static contact angles were measured by dropping 3  $\mu\text{L}$  of deionized water onto the samples. Advancing (ACA) and receding (RCA) contact angles were measured by the addition or removal of water to the droplet until an increase or decrease in the length of the baseline was observed. Contact angle hysteresis was calculated from the difference between ACA and RCA. Analysis was conducted using a Theta optical tensiometer (Biolin Scientific, Stockholm, Sweden).

**Enzymatic Degradation:** Individual samples were dried to constant weight under vacuum for a minimum of 2 days, samples were then submerged in 0.2 mg mL<sup>-1</sup> proteinase K enzyme (Sigma, St. Louis, MO) in Tris-HCL buffer (pH 8.6) with 0.2 mg mL<sup>-1</sup> sodium azide (Sigma, St. Louis, MO). Incubated samples were kept at 37 °C with agitation. The degradation solution was replaced every 24 h to maintain enzymatic activity. Samples were dried under vacuum to constant weight before final weight was established.

**Dynamic Mechanical Analysis:** DMA was performed on a DMA 8000 (Perking-Elmer) apparatus at a frequency of 1 Hz in tension mode, the temperature range was -150 to 100 °C at a rate of 1 °C min<sup>-1</sup>. Young's modulus was determined at 37 °C on sample of 10 mm  $\times$   $\approx$  6 mm  $\times$  0.05 mm.

**X-Ray Photoelectronic Spectroscopy:** X-ray photoelectronic spectroscopy was used to identify the surface chemical composition of samples. All X-ray photoelectron spectra were obtained at the National EPSRC Users' Service (NEXUS) at Newcastle University (found at: <http://www.ncl.ac.uk/nexus/>). Each sample was analyzed at three points with a maximum beam size (400  $\mu\text{m}$   $\times$  800  $\mu\text{m}$ ) with a K-alpha XPS apparatus (Thermo Scientific) equipped with a monochromatic Al K-alpha source for carbon, oxygen, nitrogen, bromine, and overview spectra. X-ray energy was 1486.68 eV at a voltage of 12 kV, current of 3 mA and power of 36 W. Analysis of the XPS results was conducted with CasaXPS version 2.3.16 (Casa Software Ltd) with adjustments for transmission and escape depth included in the VAMAS block provided by NEXUS.

**Protein Adsorption:** FN (R&D Systems) solutions of 20  $\mu\text{g}$  mL<sup>-1</sup> in DPBS were adsorbed onto samples for 1 h for all applications unless otherwise stated. Samples were rinsed with DPBS before use.

**Micro-Bicinchoninic Acid Protein Quantification:** The density of adsorbed protein was determined by measuring the amount of nonadsorbed FN. A standard curve was created via serial dilutions of an FN stock of known concentration. Samples were coated for 1 h and the remaining FN solution was transferred to 96-well plates, where the bicinchoninic acid working reagent was added (Thermo Fisher Scientific, Waltham, MA). The plate was then agitated and incubated at 37 °C for 2 h. The absorbance was read at 562 nm with a Tecan NanoQuant Infinite M200 Pro plate reader (Männedorf, Switzerland).

**In-Cell Western:** Binding domain availability on samples was examined using in-cell western (ICW). FN-coated samples were blocked with Odyssey blocking buffer (LICOR) and incubated with primary antibody, hFN7.1 (DSHB, Iowa City, IA) or mAb1937 (Millipore) in blocking buffer for 1 h. Samples were then washed five times with agitation in 0.1% v/v Tween20/PBS. IRDye 800CW antibodies were then prepared in blocking buffer and samples were incubated for 1 h. After washing as before and drying, measurements were made at 800 nm using an Odyssey system.

**C2C12 Culture:** Mouse C2C12 myoblasts were thawed and resuspended in Dulbecco's modified Eagle's medium (DMEM, high glucose, without pyruvate) with 1% v/v penicillin/streptomycin, and 20% v/v fetal bovine serum. Cells were incubated in 37 °C, 5% CO<sub>2</sub>, and harvested by trypsinization at 70% confluency.

For adhesion experiments, samples were sterilized under a UV lamp for 40 min on each side, as the samples are opaque, and coated with 20  $\mu\text{g}$  mL<sup>-1</sup> FN; negative controls were coated with PBS for 1 h. Samples were then washed with PBS and seeded with 5000 cells cm<sup>-2</sup> for 4 h and then fixed with 3.7% formaldehyde for 30 min at 4 °C. The cells were then permeabilized with 0.1% triton X-100, washed and finally blocked (PBS/BSA1%) for 30 min at room temperature. Samples were first incubated with antivinculin primary antibody (1:400), hVIN-1 (Sigma-Aldrich), in blocking buffer for 1 h at room temperature and subsequently washed with washing buffer, PBS/Tween 20 0.5%. Cy3-conjugated secondary

antibodies (Jackson ImmunoResearch) and BODIPI FL Phalloidin (Thermo Fisher Scientific) were then added for 1 h at RT. The samples were then washed and mounted with mounting medium containing DAPI (Vector Laboratories, Inc.) and visualized with a fluorescence microscope (Zeiss AxioObserver.Z1). Images were merged using ImageJ to localize nuclei and actin. Focal adhesions were analyzed using the vinculin stain images; the procedure is described by Horzum et al.<sup>[54]</sup> Images were analyzed with threshold area of  $0.5 \mu\text{m}^2$  and 0–0.99 circularity.

For differentiation assays, samples were UV sterilized; collagen controls were obtained by coating sterile coverslips with  $1 \text{ mg mL}^{-1}$  Coll (Stem Cell Technologies, Cambridge, UK) and subsequently all samples were coated with  $20 \mu\text{g mL}^{-1}$  FN for 1 h. Cells were then seeded on the samples at  $20\,000 \text{ cells cm}^{-2}$  for 3 h in DMEM +1%P/S. This was then replaced with differentiation media after 3 h and again after 2 days (DMEM +1%P/S +1%ITS-X, Life Technologies).  $10 \times 10^{-6} \text{ M}$  blebbistatin was used as contractility inhibitor and added after 3 h of culture. After 4 days of culture the cells were washed and fixed with 20:2:1 EtOH 70%/formaldehyde 37% acetic acid for 10 min at  $4^\circ\text{C}$ . Cells were then washed with PBS and blocked with 5% goat serum in PBS. Cells were then incubated with MF20-b antibody (Developmental Studies Hybridoma Bank, University of Iowa, USA) for 1 h and washed, blocked, and stained with a Cy3-conjugated antibody for 1 h at  $37^\circ\text{C}$ . Samples were then mounted with mounting medium containing DAPI and imaged. ImageJ was used to capture and merge the images. Cell density and cell differentiation were calculated using CellC image analysis software (<http://www.cs.tut.fi/sgn/csb/cellc/>).<sup>[55]</sup>

**Statistical Analysis:** Preprocessing and normalization of data are stated in the individual methods sections. Analysis of statistical differences was conducted using Student's *t*-test (Graphpad) for two sample comparison and One-way ANOVA for different groups using a Turkey HSD post hoc test to compare different groups. Differences were considered significant  $*p < 0.05$ ,  $**p < 0.01$ ,  $***p < 0.001$ ,  $****p < 0.0001$ . All data presented are mean values, error bars are standard deviation, and *n* numbers are noted in the figure captions.

## Supporting Information

Supporting Information is available from the Wiley Online Library and from the author. All the original data related to this manuscript are within the depository of the University of Glasgow with <https://doi.org/10.5525/gla.researchdata.715>.

## Acknowledgements

The authors acknowledge the EPSRC (EP/P001114/1) and MRC (MR/S005412/1) funding. The authors also acknowledge the EPSRC funding as part of the Doctoral Training Centre EP/F500424/1. This work was also funded by a grant from the UK Regenerative Medicine Platform. X-ray photoelectron spectroscopy was conducted by the National EPSRC XPS Users' Service (NEXUS), Newcastle.

## Conflict of Interest

The authors declare no conflict of interest.

## Keywords

biomimetics, cell differentiation, fibronectin, SI-ATRP, surface modification

Received: November 13, 2018

Revised: December 17, 2018

Published online: January 4, 2019

- [1] a) A. J. Rincon Lasprilla, G. A. Rueda Martinez, B. H. Lunelli, J. E. Jaimes Figueroa, A. L. Jardini, R. Maciel Filho, *Chem. Eng. Trans.* **2011**, *24*, 985; b) F. Khan, M. Tanaka, S. R. Ahmad, *J. Mater. Chem. B* **2015**, *3*, 8224.
- [2] F. Xu, X. Yang, C. Li, W. Yang, *Macromolecules* **2011**, *44*, 2371.
- [3] a) F. Khan, M. Tanaka, *Int. J. Mol. Sci.* **2018**, *19*, 17; b) P. Zhao, H. Gu, H. Mi, C. Rao, J. Fu, L.-S. Turng, *Front. Mech. Eng.* **2018**, *13*, 107.
- [4] a) Y. Zou, L. Zhang, L. Yang, F. Zhu, M. Ding, F. Lin, Z. Wang, Y. Li, *J. Controlled Release* **2018**, *273*, 160; b) J. Pyun, T. Kowalewski, K. Matyjaszewski, in *Polymer Brushes: Synthesis, Characterization and Applications* (Eds: R. C. Advincula, W. J. Brittain, K. C. Caster, J. R uhe), Wiley-VCH Verlag GmbH & Co. KGaA, Weinheim, Germany **2005**, pp. 51–68.
- [5] K. Matyjaszewski, H. Dong, W. Jakubowski, J. Pietrasik, A. Kusumo, *Langmuir* **2007**, *23*, 4528.
- [6] H. Datta, A. K. Bhowmick, N. K. Singha, *J. Polym. Sci., Part A: Polym. Chem.* **2008**, *46*, 5014.
- [7] A. Khabibullin, E. Mastan, K. Matyjaszewski, S. Zhu, *Controlled Radical Polym. Solid Surf.* **2016**, *270*, 29.
- [8] a) A. Simakova, S. E. Averick, D. Konkolewicz, K. Matyjaszewski, *Macromolecules* **2012**, *45*, 6371; b) D. J. Siegwart, J. K. Oh, K. Matyjaszewski, *Prog. Polym. Sci.* **2012**, *37*, 18; c) P. Liu, Z. X. Su, *Carbohydr. Polym.* **2005**, *62*, 159.
- [9] Q. Yu, L. M. Johnson, G. P. Lopez, *Adv. Funct. Mater.* **2014**, *24*, 3751.
- [10] A. P. Zhu, M. Zhang, J. Wu, J. Shen, *Biomaterials* **2002**, *23*, 4657.
- [11] K. Matyjaszewski, *Macromolecules* **2012**, *45*, 4015.
- [12] Y. B. Zhu, C. Y. Gao, X. Y. Liu, T. He, J. C. Shen, *Tissue Eng.* **2004**, *10*, 53.
- [13] H. Tsuji, M. Ogiwara, S. K. Saha, T. Sakaki, *Biomacromolecules* **2006**, *7*, 380.
- [14] Y. He, W. Wang, J. Ding, *Chin. Sci. Bull.* **2013**, *58*, 2404.
- [15] M. Cantini, C. Gonz alez-Garc a, V. Llopis-Hern andez, M. Salmer on-S anchez, in *Proteins at Interfaces III State of the Art, ACS Symposium Series* (Eds: T. Horbett, J. L. Brash, W. Norde), American Chemical Society, Washington DC, USA **2012**, pp. 471–496.
- [16] a) V. Llopis-Hernandez, P. Rico, D. Moratal, G. Altankov, M. Salmeron-Sanchez, *BioRes. Open Access* **2013**, *2*, 364; b) M. Salmeron-Sanchez, P. Rico, D. Moratal, T. T. Lee, J. E. Schwarzbauer, A. J. Garcia, *Biomaterials* **2011**, *32*, 2099.
- [17] a) F. A. Vanterpool, M. Cantini, F. P. Seib, M. Salmeron-Sanchez, *BioRes. Open Access* **2014**, *3*, 286; b) F. Bathawab, M. Bennett, M. Cantini, J. Reboud, M. J. Dalby, M. Salmeron-Sanchez, *Langmuir* **2016**, *32*, 800.
- [18] P. Lozano Picazo, M. Perez Garnes, C. Martinez Ramos, A. Valles-Lluch, M. Monleon Pradas, *Macromol. Biosci.* **2015**, *15*, 229.
- [19] A. S. Schulz, H. Gojzewski, J. Huskens, W. L. Vos, G. J. Vancso, *Polym. Adv. Technol.* **2018**, *29*, 806.
- [20] a) M. Muellner, S. J. Dodds, N. Tri-Hung, D. Senyschyn, C. J. H. Porter, B. J. Boyd, F. Caruso, *ACS Nano* **2015**, *9*, 1294; b) W. G. Kreyling, A. M. Abdelmonem, Z. Ali, F. Alves, M. Geiser, N. Haberl, R. Hartmann, S. Hirn, D. Jimenez de Aberasturi, K. Kantner, G. Khadem-Saba, J.-M. Montenegro, J. Rejman, T. Rojo, I. Ruiz de Larramendi, R. Ufartes, A. Wenk, W. J. Parak, *Nanotechnol.* **2015**, *10*, 619.
- [21] R. Pankov, K. M. Yamada, *J. Cell Sci.* **2002**, *115*, 3861.
- [22] a) A. J. Garcia, M. D. Vega, D. Boettiger, *Mol. Biol. Cell* **1999**, *10*, 785; b) F. Gattazzo, A. Urciuolo, P. Bonaldo, *Biochim. Biophys. Acta, Gen. Subj.* **2014**, *1840*, 2506; c) J. J. Hay, A. Rodrigo-Navarro, K. Hassi, V. Moulisova, M. J. Dalby, M. Salmeron-Sanchez, *Sci. Rep.* **2016**, *6*, 21809.
- [23] Y. Zhu, C. Gao, X. Liu, J. Shen, *Biomacromolecules* **2002**, *3*, 1312.

- [24] a) R. T. MacDonald, S. P. McCarthy, R. A. Gross, *Macromolecules* **1996**, *29*, 7356; b) Y. Tokiwa, B. P. Calabia, *Appl. Microbiol. Biotechnol.* **2006**, *72*, 244; c) X. Hu, T. Su, P. Li, Z. Wang, *Polym. Bull.* **2017**, *75*, 533.
- [25] E. P. S. Gee, D. Yueksel, C. M. Stultz, D. E. Ingber, *J. Biol. Chem.* **2013**, *288*, 21329.
- [26] P. Roach, D. Eglin, K. Rohde, C. C. Perry, *J. Mater. Sci.: Mater. Med.* **2007**, *18*, 1263.
- [27] M. J. Dalby, N. Gadegaard, R. O. C. Oreffo, *Nat. Mater.* **2014**, *13*, 558.
- [28] O. Nedela, P. Slepicka, V. Svorcik, *Materials* **2017**, *10*, 1115.
- [29] E. N. Mpoyi, M. Cantini, P. M. Reynolds, N. Gadegaard, M. J. Dalby, M. Salmeron-Sanchez, *ACS Nano* **2016**, *10*, 6638.
- [30] M. Cantini, P. Rico, D. Moratal, M. Salmeron-Sanchez, *Soft Matter* **2012**, *8*, 5575.
- [31] P. K. Chu, J. Y. Chen, L. P. Wang, N. Huang, *Mater. Sci. Eng.: R* **2002**, *36*, 143.
- [32] J. O. Zoppe, N. C. Ataman, P. Mocny, J. Wang, J. Moraes, H.-A. Klok, *Chem. Rev.* **2017**, *117*, 1105.
- [33] H. Yasuda, T. Yasuda, *J. Polym. Sci., Part A: Polym. Chem.* **2000**, *38*, 943.
- [34] H. Ma, M. Textor, R. L. Clark, A. Chilkoti, *Biointerphases* **2006**, *1*, 35.
- [35] a) S. Ohno, K. Matyjaszewski, *J. Polym. Sci., Part A: Polym. Chem.* **2006**, *44*, 5454; b) C. Kang, R. M. Crockett, N. D. Spencer, *Macromolecules* **2014**, *47*, 269; c) D. Q. Xiao, M. J. Wirth, *Macromolecules* **2002**, *35*, 2919; d) H. Shinoda, K. Matyjaszewski, *Macromolecules* **2001**, *34*, 6243.
- [36] F. J. Xu, J. P. Zhao, E. T. Kang, K. G. Neoh, *Ind. Eng. Chem. Res.* **2007**, *46*, 4866.
- [37] a) T. Zhou, H. Qi, L. Han, D. Barbash, C. Y. Li, *Nat. Commun.* **2016**, *7*, 11119; b) W. Guo, J. Zhu, Z. Cheng, Z. Zhang, X. Zhu, *ACS Appl. Mater. Interfaces* **2011**, *3*, 1675; c) M. Ignatova, S. Voccia, B. Gilbert, N. Markova, P. S. Mercuri, M. Galleni, V. Sciannamea, S. Lenoir, D. Cossement, R. Gouttebaron, R. Jérôme, C. Jérôme, *Langmuir* **2004**, *20*, 10718; d) E. Taran, B. Donose, K. Higashitani, A. D. Asandei, D. Scutaru, N. Hurduc, *Eur. Polym. J.* **2006**, *42*, 119.
- [38] F. Liu, C.-H. Du, B.-K. Zhu, Y.-Y. Xu, *Polymer* **2007**, *48*, 2910.
- [39] B. D. Ulery, L. S. Nair, C. T. Laurencin, *J. Polym. Sci., Part B: Polym. Phys.* **2011**, *49*, 832.
- [40] a) E. Saito, E. E. Liao, W.-W. Hu, P. H. Krebsbach, S. J. Hollister, *J. Tissue Eng. Regen. Med.* **2013**, *7*, 99; b) Z. Wang, Y. Wang, Y. Ito, P. Zhang, X. Chen, *Sci. Rep.* **2016**, *6*, 20770; c) I. Armentano, M. Dottori, E. Fortunati, S. Mattioli, J. M. Kenny, *Polym. Degrad. Stab.* **2010**, *95*, 2126.
- [41] M. Cantini, K. Gomide, V. Moulisova, C. González-García, M. Salmerón-Sánchez, *Adv. Biosyst.* **2017**, *1*, 1700047.
- [42] J. Pelta, H. Berry, G. C. Fadda, E. Pauthe, D. Lairez, *Biochemistry* **2000**, *39*, 5146.
- [43] D. Gugutkov, C. Gonzalez-Garcia, J. C. Rodríguez Hernández, G. Altankov, M. Salmerón-Sánchez, *Langmuir* **2009**, *25*, 10893.
- [44] P. Rico Tortosa, M. Cantini, G. Altankov, M. Salmeron-Sanchez, in *Polymers in Regenerative Medicine: Biomedical Applications from Nano- to Macro-Structures* (Eds: M. Monleón Pradas, M. J. Vicent), John Wiley & Sons, Inc., Hoboken, New Jersey **2014**, pp. 91–146.
- [45] a) J. E. Schwarzbauer, D. W. DeSimone, *Cold Spring Harbor Perspect. Biol.* **2011**, *3*, a005041; b) M. M. Martino, F. Tortelli, M. Mochizuki, S. Traub, D. Ben-David, G. A. Kuhn, R. Mueller, E. Livne, S. A. Eming, J. A. Hubbell, *Sci. Transl. Med.* **2011**, *3*, 100ra89.
- [46] a) B. G. Keselowsky, D. M. Collard, A. J. Garcia, *J. Biomed. Mater. Res., Part A* **2003**, *66A*, 247; b) B. G. Keselowsky, D. M. Collard, A. J. Garcia, *Biomaterials* **2004**, *25*, 5947; c) B. G. Keselowsky, D. M. Collard, A. J. Garcia, *Proc. Natl. Acad. Sci. USA* **2005**, *102*, 5953.
- [47] V. Llopis-Hernandez, M. Cantini, C. Gonzalez-Garcia, Z. A. Cheng, J. Yang, P. M. Tsimbouri, A. J. Garcia, M. J. Dalby, M. Salmeron-Sanchez, *Sci. Adv.* **2016**, *2*, e1600188.
- [48] J. Ballester-Beltran, D. Moratal, M. Lebourg, M. Salmeron-Sanchez, *Biomater. Sci.* **2014**, *2*, 381.
- [49] S. D. Redick, D. L. Settles, G. Briscoe, H. P. Erickson, *J. Cell Biol.* **2000**, *149*, 521.
- [50] K. Tanaka, K. Sato, T. Yoshida, T. Fukuda, K. Hanamura, N. Kojima, T. Shirao, T. Yanagawa, H. Watanabe, *Muscle Nerve* **2011**, *44*, 968.
- [51] a) J. S. Allingham, R. Smith, I. Rayment, *Nat. Struct. Mol. Biol.* **2005**, *12*, 378; b) M. Kovacs, J. Toth, C. Hetenyi, A. Malnasi-Csizmadia, J. R. Sellers, *J. Biol. Chem.* **2004**, *279*, 35557.
- [52] Y. Cai, O. Rossier, N. C. Gauthier, N. Biais, M.-A. Fardin, X. Zhang, L. W. Miller, B. Ladoux, V. W. Cornish, M. P. Sheetz, *J. Cell Sci.* **2010**, *123*, 413.
- [53] C. Gonzalez-Garcia, D. Moratal, R. O. C. Oreffo, M. J. Dalby, M. Salmeron-Sanchez, *Integr. Biol.* **2012**, *4*, 531.
- [54] U. Horzum, B. Ozdil, D. Pesen-Okvur, *MethodsX* **2014**, *1*, 56.
- [55] J. Selinummi, J. Seppala, O. Yli-Harja, J. A. Puyhakka, *BioTechniques* **2005**, *39*, 859.
- [56] D. J. Leahy, I. Aukhil, H. P. Erickson, *Cell* **1996**, *84*, 155.